Appendixes A

Physical Structure-Based Small Signal Modeling for GaN Fin-HEMTs

Ziyue Zhao, Yang Lu*, Chupeng Yi, Ting Feng, Xin Liu, Wei Zhao, Guanghai Yao, Yilin Chen*, Xiaohua Ma, and Yue Hao

National Engineering Research Center of Wide Band-gap Semiconductor, Xidian University, Xi'an 710071, China

Abstract In this work, a comprehensive analysis was conducted on the structure and mechanism of Gallium nitride (GaN) -based Fin-High Electron Mobility Transistors (HEMTs). A physical structure-based small signal model (named PS-model) and a parameter extraction method of Fin-HEMTs were proposed, which demonstrated high fitting accuracy. The PS-model introduces two significant innovations. Firstly, in this model, the parasitic capacitance (C_g) between the gate and the two-dimensional electron gas (2DEG) was taken into account, which is calculated using simulation techniques and conformal transformation. The accuracy of parameter extraction was significantly enhanced due to this revision. Secondly, the parasitic effects between the trench region and the 2DEG was introduced in the PS-model, incorporating parallel capacitors namely C_{gs_trench} and C_{gd_trench}. This enabled the effective capture of the distribution effects introduced by the Fin structure. Finally, parameter extraction and analysis under multiple biases were performed using the new model, and the mechanism and characteristics of Fin-HEMTs were explained and analyzed. Simultaneously, fitting results validated the advancement and accuracy of the PS-model. The establishment of the model will further promote the application of Fin-HEMT in circuit design.

Keywords GaN-based, physical structure-based, Fin-HEMT, small signal model

1 Introduction

Gallium nitride (GaN) based high electron mobility transistors (HEMTs) have been extremely attractive in high-power, high-voltage, and high-frequency fields due to their many merits, including high power output, high operating frequency, and high breakdown electric field [1]–[4]. In order to further improve device performance, the device follows the principle of proportional reduction to reduce device size [5]. However, reducing the gate length (L_g) to the deep sub-micron levels leads to short-channel effects (SCEs), which is mainly due to the decline in gate control capability. Benefiting from their advanced tri-gate structure, Fin-HEMTs can significantly enhance gate control and effectively suppress device performance degradation caused by SCEs [6]-[8]. The structure of the Fin-HEMTs is shown in Figure 1, which exhibits a periodic nanochannel structure by using the etching process. The introduction of the side-wall gate in the Fin-HEMTs can effectively increase the control area and ability of the gate. Therefore, the gate is the core part of Fin-HEMTs.

In order to promote the application of GaN-based Fin-HEMTs in high-power and high frequency fields, the establishment of accurate small signal models (SSMs) plays a crucial role [9]-[12]. The SSM of a device not only characterizes the structural characteristics, but also serves as the foundation for the large signal model, which is a link between the device and the circuit [13].

*Corresponding author (email: luyang@xidian.edu.cn; chenyilin@xidian.edu.cn)

The traditional models for GaN Fin-HEMTs do not consider the influence of gate capacitance and distribution effect, so the S-parameter fitting accuracy will be reduced. Therefore, this work aims to establish an accurate SSM for GaN-based Fin-HEMTs based on the characteristics of the gate, so that Fin-HEMTs can be better applied in circuit design.

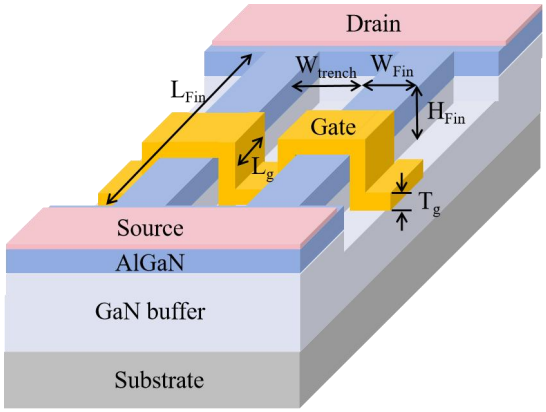

Figure 1 The structure of the GaN-based Fin-HEMTs.

2 The structure of the GaN-based Fin-HEMTs.

The GaN Fin-HEMTs investigated in this work were made in Xidian University [14]-[15], and the structure of the device is shown in Figure 1. The epitaxial heterostructure which consists of a 22 nm $Al_{0.3}Ga_{0.7}N$ barrier layer (T_{AlGaN}=22nm), a 2 μm GaN buffer layer, and a 100 nm AlN nuclear layer were grown on a SiC substrate. The device fabrication processes are shown in the work [15]. The oxidation process is performed before the gate metal [14]. The gate electrode is deposited by of Ni/Au, and the gate thickness (T_g) is 45/400 nm. W_{Fin}, L_{Fin}, and H_{Fin} represent the width, length, and height of the Fin in one period, respectively. W_{trench} indicates the width of the trench region in one period. The gate length (L_g), the distance of gate–drain (L_{gs}) and source–drain (L_{sd}) are 0.2, 0.3 and 3 μm, respectively.

In order to compare the devices performance and verify the model accuracy, we fixed the H_{Fin}, L_{Fin}, and W_{trench} of the device, and fabricated Fin-HEMTs with the W_{Fin} of 200nm, 250nm, and 300nm, respectively. The key parameters of the device are shown in Table 1.

Table 1 The value of the device's structural parameters

Parameter	Value	Parameter	Value
H_{Fin}	30 nm	L_g	0.2 μm
W_{trench}	150 nm	T_g	445 nm
L_{gs}	0.3 μm	L_{sd}	3 μm

3 Modeling of Fin-HEMTs

3.1 Simulation of the Device

The electron concentration distribution was simulated by using Silvaco TCAD in order to isolate the control ability of the side-wall gate. The performance of the device with three different W_{Fin} (200nm, 250nm, 300nm) was simulated. The parameters of the device structure are the same as

the fabricated ones.

Figure 2(a)–(c) shows the electron concentration distribution of Fin-HEMTs with W_{Fin} of 200, 250, 300 nm respectively, under a gate voltage (V_{gs}) and drain voltage (V_{ds}) of 0V. It can be found that the Schottky contact of the side-wall gate can effectively deplete the 2DEG in the channel along the Fin width direction, assisting the top-gate to control the carrier in the channel, and improve the control ability of the whole gate. It can be seen that with the decrease of W_{Fin}, the control ratio of the side-wall gate to the carrier increases.

Figure 2(d) shows the electron concentration distribution of cross sections along the W_{Fin} (200, 250, 300 nm) at the heterojunction interface, which reflected the influence of the side-wall gate on the carrier concentration. It can be seen that along the gate width (W_g) direction, the electron concentration near the side-wall gate is very low due to the depletion caused by the Schottky contact of side-wall gates. Therefore, the electron concentration distribution in Figure 2(d) can be divided into three regions along the width direction of the gate. The depletion width of the side-wall gate on one side is about 50 nm (W_{side}), and the width affected by the top gate is $W_{top}=W_{Fin}-2\times W_{side}$. That is, when the W_{Fin} is less than 100 nm, the Fin is affected by the side-wall gates only.

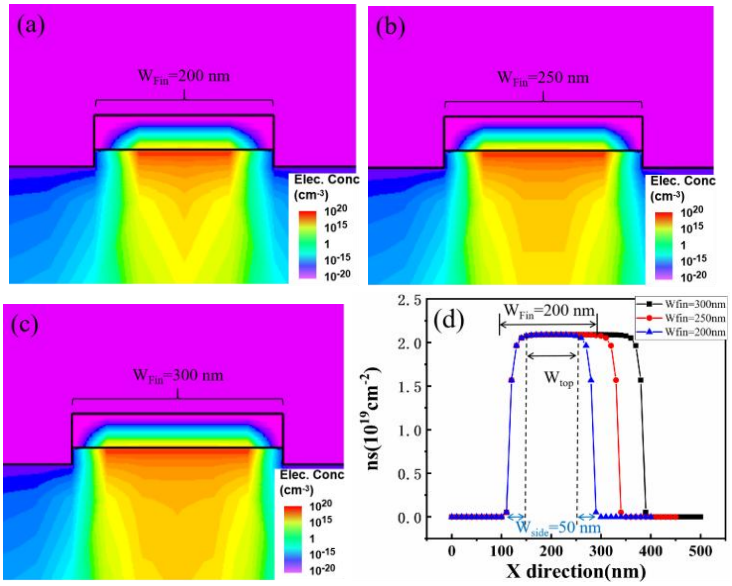

Figure 2 (a) – (c) The electron concentration distribution of Fin HEMTs with W_{Fin} of 200, 250, 300 nm respectively at gate voltage and drain voltage of 0V. (d) The electron concentration distribution of cross sections along the W_{Fin} (200, 250, 300 nm) at the heterojunction interface of the device.

3.2 The Calculation of Gate Capacitance

The most significant feature of the Fin-HEMTs compared to the planar HEMTs is an introduction by the side-wall gate. For the planar HEMTs, only the top-gate exists. Therefore, the parasitic gate capacitance (C_g) only caused by the top-gate and does not significantly affect the nonlinear characteristics of the intrinsic capacitance (C_{gs} and C_{gd}). So, the influence of the C_g is distributed in the intrinsic capacitance C_{gs} and C_{gd} in the SSM of the planar HEMTs. For the Fin-HEMTs, side-wall gates induce a more pronounced C_g [15]. At the same time, the parasitic capacitances are also generated between the trench region and 2DEG, which affects C_{gs} and C_{gd} directly. Therefore, in order to build an accurate Fin-HEMT model, it is necessary to consider the influence of C_g and the trench region.

Because of the special characteristics of the Fin-HEMTs, C_g is composed of parasitic

capacitance from the top-gate (C_{g_top}) and the side-wall gate (C_{g_side}). The C_{g_top} is primarily determined by the physical structure of the device and represents the capacitance between the top-gate and the channel, and the C_{g_side} represents the capacitance between the side-wall gate and the 2DEG. Due to the existence of a multi-period Fin structure in the gate-width direction, the side-wall gate will introduce an additional large parasitic gate capacitance, so the C_g of the Fin-HEMT will be larger than that of the planar device. The increase of C_g will reduce the accuracy of Fin-HEMTs intrinsic capacitors C_{gs} and C_{gd} in traditional modeling. Therefore, C_g needs to be calculated and de-embedded before the extraction of intrinsic parameters for Fin-HEMTs.

The formula of the C_{g_top} is shown in (1). It is worth noting that due to the influence of the side-wall gate [16]-[17], the effective area of the top gate is no longer $L_g \times W_{Fin}$, and it will be changed to $L_g \times W_{top}$.

$$C_{g\_top} = \varepsilon_{AlGaN} \frac{L_g \times W_{top}}{T_{AlGaN}} \tag{1}$$

Then the C_{g_side} can be calculated by the conformal transformation [18]-[19]. The C_{g_side} is the sum of C_{g_up} and C_{g_down} which is shown in Figure 3. In the figure, T_{ox} is 3 nm [14]. Each of these capacitances (C_{g_up} and C_{g_down}) has an inner capacitance and outer capacitance [18].

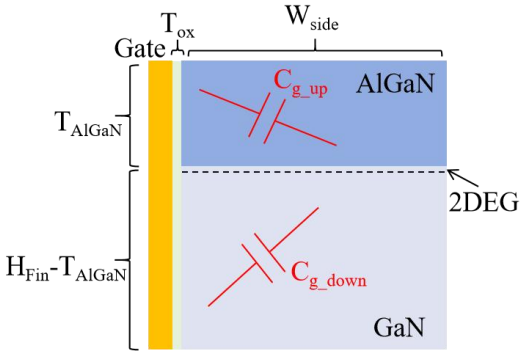

Figure 3 Structure diagram of the gate for C_{side} calculations, where T_{AlGaN} is 22 nm, T_{ox} is 3 nm, H_{Fin} is 30 nm, and W_{side} is 50 nm.

Therefore, C_{g_side} is calculated by the formula (2).

$$\begin{aligned}\frac{C_{g\_side}}{L_g} = {} & \varepsilon_{AlGaN}\left(\frac{K'\left(k_{up\_in}\right)}{K\left(k_{up\_in}\right)} + \frac{K'\left(k_{up\_out}\right)}{K\left(k_{up\_out}\right)}\right) \\ & + \varepsilon_{GaN}\left(\frac{K'\left(k_{down\_in}\right)}{K\left(k_{down\_in}\right)} + \frac{K'\left(k_{down\_out}\right)}{K\left(k_{down\_out}\right)}\right)\end{aligned} \tag{2}$$

$$k_{up\_in} = \frac{T_{ox}}{T_{ox} + W_{side}} \sqrt{\frac{\left(T_{ox} + W_{side}\right)^2 + T_{AlGaN}^2}{T_{ox}^2 + T_{AlGaN}^2}} \tag{3}$$

$$k_{up\_out} = \sqrt{\frac{T_{ox}^{2/3}\left(\left(T_{ox} + W_{side}\right)^{2/3} + T_{AlGaN}^{2/3}\right)}{\left(T_{ox} + W_{side}\right)^{2/3}\left(T_{ox}^{2/3} + T_{AlGaN}^{2/3}\right)}} \tag{4}$$

Where K(x) represents the complete elliptic integral of the first class [16], which can be calculated by MATLAB R2023a rapidly. And $K'(x)=K(x')$, x' represents the complementary modulus of x. The formula for x' is shown in (5).

$$x' = \sqrt{1 - x^2} \tag{5}$$

It is worth noting that in the calculation of C_{g_side}, the state of the 2DEG varies under different biases. Therefore, in theory, C_{g_side} should change with biases. However, to simplify the model, this work base the calculation on the device structure and neglect the nonlinear dependence of C_{g_side} on biases. The nonlinear characteristics of this part are instead incorporated into the intrinsic capacitance C_{gs} and C_{gd}.

Finally, the C_g in a cycle can be calculated by the formula (6). The total C_g is determined by the W_g and the Fin period (W_{Fin}+W_{trench}) which is calculated by the formula (7).

$$C_{g\_single} = C_{g\_top} + 2 \times C_{g\_side} \tag{6}$$

$$C_{g\_total} = C_{g\_single} \times \left(\frac{W_g}{W_{Fin} + W_{trench}} \right) \tag{7}$$

The C_g in a single cycle is calculated with different W_{Fin}, and the results calculated by the formula (1)-(6) are shown in Figure 4. When W_{Fin} is greater than or equal to 100 nm, the value of W_{side} is 50 nm; when W_{Fin} is less than 100 nm, W_{side} equals $W_{Fin}/2$. When W_{Fin} is less than or equal to 100 nm, the influence of C_{g_top} can be disregarded. Since the W_{trench} of the device is fixed, different W_{Fin} correspond to different Fin cycles for the device with 100 μm gate width. When the W_{Fin} is 300 nm, the number of the Fin cycle is about 222, so C_{g_total} is 56.12 fF.

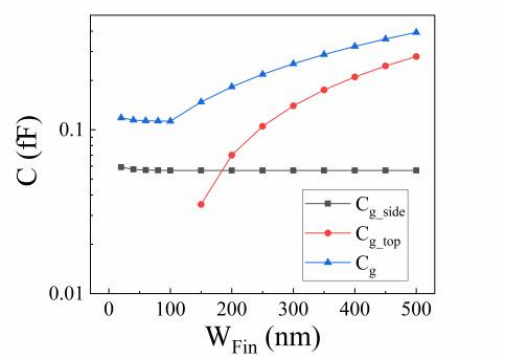

Figure 4 The C_g in a cell with different W_{Fin}. The W_{Fin} is from 20 nm to 500 nm. The C_g is consisted from C_{g_top} and C_{g_side}. C_{g_top} is represented by the red curve, C_{g_side} is represented by the black curve, and C_g is represented by the blue curve.

For the trench region, the gate shows a vertical relationship with 2DEG. The capacitance between the gate in trench region and 2DEG can be calculated by the above method. The top view of the device is shown in Figure 5. The capacitance between the trench region and the 2DEG in the gate-source region is defined as C_{gs_trench}, and the capacitance between the trench region and the 2DEG in the gate-drain region is defined as C_{gd_trench}. Therefore, the C_{gs_trench} can be calculated by the formula (8)-(10), and the calculation of C_{gd_trench} is similar for C_{gs_trench}. C_{gs_trench} and C_{gd_trench} are influenced by the 2DEG state of the device, so these two capacitance values will vary with the device's bias. Therefore, C_{gs_trench} and C_{gd_trench} are intrinsic parameters of the model.

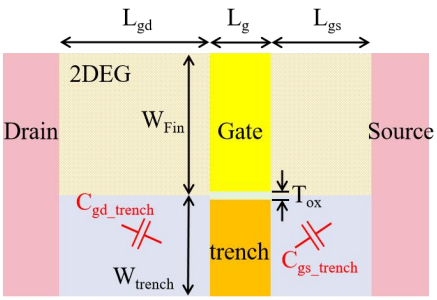

Figure 5 The top view of the device in a cycle and the relationship of the C_{gs_trench} and the C_{gd_trench}.

$$k_{gs\_in} = \frac{T_{ox}}{T_{ox} + W_{trench}} \sqrt{\frac{\left(T_{ox} + W_{trench}\right)^2 + L_{gs}^2}{T_{ox}^2 + L_{gs}^2}} \tag{8}$$

$$k_{gs\_out} = \sqrt{\frac{T_{ox}^{2/3}\left(\left(T_{ox} + W_{trench}\right)^{2/3} + L_{gs}^{2/3}\right)}{\left(T_{ox} + W_{trench}\right)^{2/3}\left(T_{ox}^{2/3} + L_{gs}^{2/3}\right)}} \tag{9}$$

$$\frac{C_{gs\_trench}}{T_g} = \varepsilon_{air}\left(\frac{K'\left(k_{gs\_in}\right)}{K\left(k_{gs\_in}\right)} + \frac{K'\left(k_{gs\_out}\right)}{K\left(k_{gs\_out}\right)}\right) \tag{10}$$

It is important to note that the parameter values of C_{gs_trench} and C_{gd_trench} are influenced by the state of the 2DEG. In this work, these values are calculated solely based on the physical structure of the device, without considering the impact of bias. This simplification introduces some degree of error in the model parameters. However, accurately characterizing the influence of bias on capacitance through measurements or TCAD simulations is challenging. Therefore, using Equations (8)-(10), C_{gs_trench} and C_{gd_trench} can be quickly obtained as ideal initial values, and an optimization algorithm can subsequently be applied to eliminate the errors introduced under different biases.

Take the W_{Fin} (300nm) as an example. By the above means, the values of C_{gs_trench} and C_{gd_trench} are shown in Table 2. It should be noted that due to the variation of the 2DEG concentration under different biases, the effective values of W_{trench}, L_{gs}, and L_{gd} will fluctuate, although they have clear physical meanings. However, the value of C_{gs_trench} and C_{gd_trench} in the table is an ideal initial value, the error caused by the change of the bias can be eliminated by the single optimization algorithm.

Table 2 The value of parameters

Parameter	Value	Parameter	Value
C_{gs_trench}	$1.5573e^{-2}$ fF	C_{gd_trench}	$1.5643e^{-2}$ fF

3.3 The establishment of the PS-model

The PS-model is established based on the physical structure of the Fin-HEMT, and the structure of the model is shown in Figure 6(a). Compared with the traditional model, the PS-model introduces three new parameters, C_g, C_{gs_trench}, and C_{gd_trench}. The equivalent circuit topology of the device is shown in Figure 6(b). In the model, the parameters inside the dotted are intrinsic parameters, and the others are parasitic parameters.

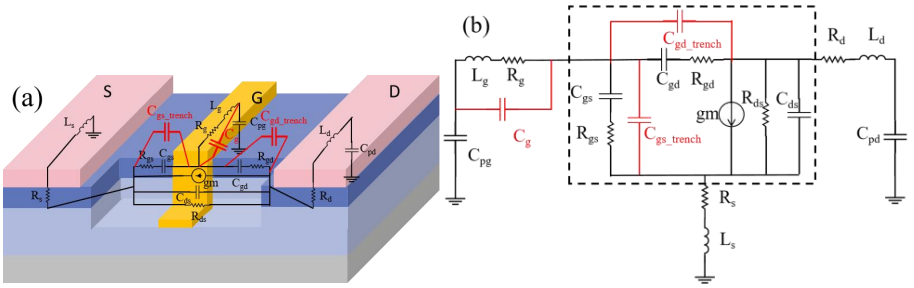

Figure 6 (a) The stereogram of the device in a cell and the structure of the SSM. (b) The equivalent circuit topology of the device.

R_g, R_d, and R_s represent the parasitic resistance generated by the electrode, L_g, L_d, and L_s represent the parasitic inductance generated by the metal, and C_{pg} and C_{pd} represent the parasitic capacitance of the electrode pad. Since C_g represents the parasitic capacitance between the gate and 2DEG, C_g should be in parallel with R_g and L_g.

C_{ds} characterizes capacitance of the channel between the source electrode and the drain electrode. And R_{ds} is the intrinsic resistance between them. gm represents the intrinsic transconductance of the device. C_{gs} and C_{gd} represent the capacitance between the gate-source and the gate-drain in the channel, respectively. Due to the existence of the path within the heterojunction in the Fin, R_{gs} and R_{gd} are needed to represent the quasi-static resistance between the gate-source and the gate-drain. Parallel capacitors C_{gs_trench} and C_{gd_trench} are introduced to represent the capacitance in the trench region. On the one hand, the introduction of the C_{gs_trench} and C_{gd_trench} can improve the fitting of the distribution effect of the device. On the other hand, it can fit the capacitance effect of the trench region of the device. In order to more intuitively represent the relationship between C_{gd} and C_{gd_trench}, Figure 7 shows a stereogram of the device between the gate-drain, and the effect of the gate–source is similar to the gate-drain.

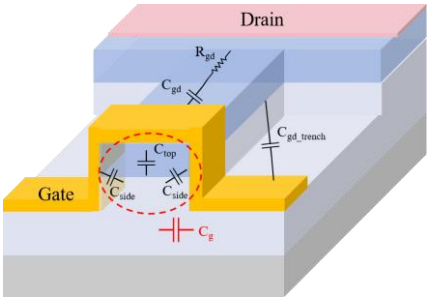

Figure 7 The stereogram of the device between the gate-drain, and the figure shows the specific locations of C_g and C_{gd_trench}.

To get the value of each parameter, the parasitic parameters of the device are extracted by the traditional Cold-FET method [20]-[22]. Considering the error of parameter value extraction caused by the introduction of C_g, the fitting accuracy of S-parameter in “Cold” state of the device is improved by one more optimization. The intrinsic Y parameter (Y_{int}) is obtained by de-embedding. Due to the introduction of C_g, the de-embedding method is different from the traditional way, which is represented by Figure 8. It is worth noting that in order to simplify the calculation, the parallel structure composed of C_g, R_g, and L_g needs to be equivalent to the series structure of L'_g and R'_g.

$$R_g^{'} = a / c \tag{11}$$

$$L_g^{'} = b / c \tag{12}$$

$$a = R_g \left(R_g^2 + \omega^2 L_g^2 \right) \tag{13}$$

$$b = \left(R_g^2 + \omega^2 L_g^2 \right) \left(C_g R_g^2 - L_g + \omega^2 C_g L_g^2 \right) \tag{14}$$

$$c = R_g^2 + \omega^2 \left(C_g R_g^2 - L_g + \omega^2 C_g L_g^2 \right)^2 \tag{15}$$

Then,

$$Y_{\text{int}11} = \left(R_{gs} + \left(j\omega C_{gs} \right)^{-1} \right)^{-1} + \left(R_{gd} + \left(j\omega C_{gd} \right)^{-1} \right)^{-1} + j\omega \left(C_{gs\_trench} + C_{gd\_trench} \right) \tag{16}$$

$$Y_{\text{int}12} = -\left(R_{gd} + \left(j\omega C_{gd} \right)^{-1} \right)^{-1} - j\omega C_{gd\_trench} \tag{17}$$

$$Y_{\text{int}21} = -\left(R_{gd} + \left(j\omega C_{gd} \right)^{-1} \right)^{-1} - j\omega C_{gd\_trench} + gm \tag{18}$$

$$Y_{\text{int}22} = \left(R_{gd} + \left(j\omega C_{gd} \right)^{-1} \right)^{-1} + j\omega \left(C_{gd\_trench} + C_{ds} \right) + \frac{1}{R_{ds}} \tag{19}$$

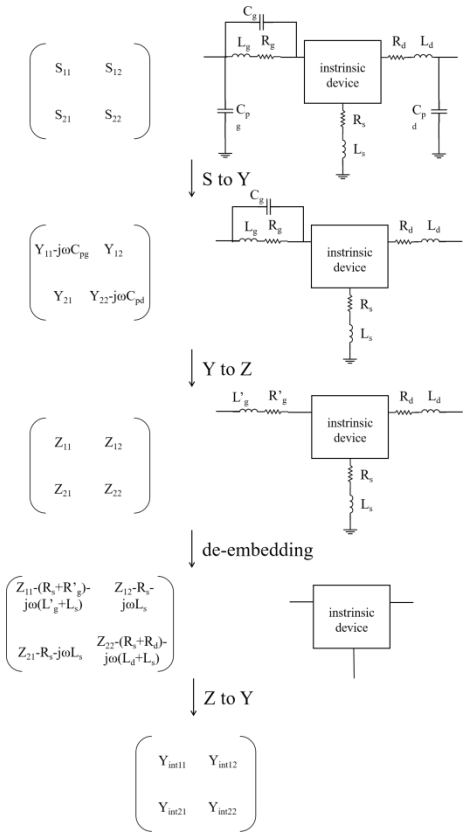

Figure 8 Method for extracting the device intrinsic Y matrix.

Through the mutual calculation between (16) and (17), it can be obtained:

$$Y_{\text{int11}} + Y_{\text{int12}} = \frac{\omega^2 C_{gs}^2 R_{gs}}{1+\omega^2 C_{gs}^2 R_{gs}^2} + j\omega\left(C_{gs\_trench} + \frac{C_{gs}}{1+\omega^2 C_{gs}^2 R_{gs}^2} \right) \tag{20}$$

By calculating the slope and intercept between ω^2/real(Y_{int11}+Y_{int12}) and ω^2, the value of C_{gs} and R_{gs} can be obtained respectively. Similarly, the values of C_{gd} and R_{gd} can be obtained based on ω^2/-real(Y_{int12}). And through the previous calculation, the values of C_{gd_trench} and C_{gs_trench} have been obtained.

Finally, based on (17) and (18), the values of gm, C_{ds}, and R_{ds} ($1/g_{ds}$) can be obtained.

Through the above steps, the initial value of the parameters can be extracted.

4 Results

After the calculation and extraction of model parameters, the model has been able to achieve an ideal fitting. In order to further improve the accuracy, and the initial values of the model parameters are relatively ideal, the final parameters can be obtained through a single gradient optimization. The optimization algorithm not only eliminates errors introduced during the parameter extraction process but also compensates for the effects of bias variations on the values of C_{gs_trench} and C_{gd_trench}. The performance of the optimization is determined not only by the effectiveness of the model topology but also by the quality of the initial parameter estimates. High-quality initial parameters not only enhance the efficiency of model development but also significantly improve the accuracy of model fitting. Taking biases (-1.6V, 10V) and (-3V, 15V) as examples, the values of each parameter are shown in Table 3 and Table 4, and the fitting results are shown in Figure 9. The frequency range for the S-parameters is 1-30 GHz, and the testing step is 0.1 GHz. These two bias conditions are commonly used for the device, representing that the device is in Class A and Class AB, respectively. In order to express the advancement of the PS-model more directly, the fitting results of the PS-Model are also compared with those of traditional model [24] in Figure 9. In the figure, black curves represent the measured S-parameters, red curves represent the S-parameters fitting results using the PS-model, and blue curves represent the fitting results using the traditional GaN HEMT model [24]. In [24], an integrated parameter extraction method was employed that takes into account the influence of parasitic inductance on the extraction of parasitic capacitance, enabling rapid and accurate determination of model parameters. Therefore, the parameter extraction method in [24] effectively demonstrates the fitting capability of the conventional model's topology, as evidenced by the blue curve in Figure 9 achieving an ideal fitting result. Based on this, a comparison with the fitting results of the PS-model further underscores its advanced nature.

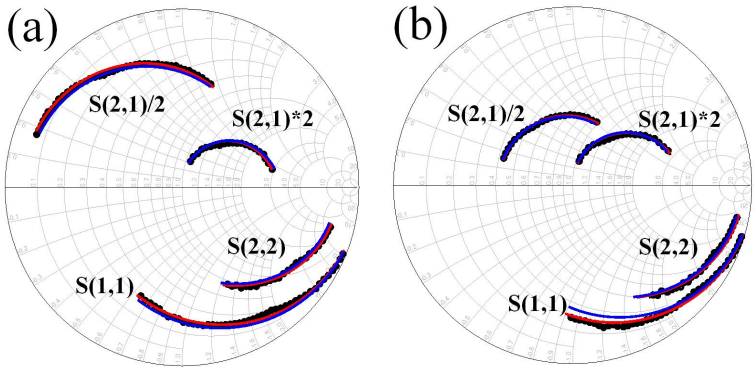

Figure 9 (a) The fitting result of the PS-model under (-1.6V, 10V). (b) The fitting result of the PS-model under (-3V,15V). In the figure, black curves represent the measured S-parameters, red curves represent the S-parameters fitting results using the PS-model, and blue curves represent the fitting results using the traditional GaN HEMT model. The frequency range for the S-parameters is 1-30 GHz, and the testing step is 0.1 GHz.

At the same time, in order to evaluate the fitting accuracy of the model, the fitting errors of both the PS-model and the traditional model were calculated by the method used in reference [21], and the calculation results were shown in Table 5. It can be seen that the PS-model for GaN-based Fin-HEMT can achieve ideal fitting. From the fitting results in Table 5, it can be seen that the model topology and parameter extraction method in reference [21] result in an S-parameter fitting error of about 2.5%, which has already achieved a relatively ideal fitting result. The PS-model proposed in this work, relying on an improved model topology and a more ideal parameter initial value extraction, can effectively further improve the fitting accuracy of the S-parameters. The enhancement in fitting not only proves the advanced nature of the improved topology of the PS-model, but also validates the effectiveness of the parameter extraction method used in this work.

Table 3 The value of the model's parameters under (-1.6V, 10V)

Parameter	Value	Parameter	Value
C_{pg}	1.58e^{-15} F	C_{pd}	1.58e^{-15} F
R_g	2.29 Ω	R_d	7.41 Ω
R_s	2.09 Ω	L_g	6.84e^{-11} H
L_s	1.39e^{-11} H	L_d	6.28e^{-11} H
C_g	56.12e^{-15} F	C_{gs}	7.49e^{-14} F
R_{gs}	1.58 Ω	C_{gs_trench}	4.23e^{-14} F
C_{gd}	2.82e^{-14} F	R_{gd}	7.31 Ω
C_{gd_trench}	1.54e^{-14} F	C_{ds}	2.80e^{-14} F
g_{ds}	1.00e^{-3} S	gm	2.00e^{-2} S

Table 4 The value of the model's parameters under (-3V, 15V)

Parameter	Value	Parameter	Value
C_{gs}	6.15e^{-14} F	R_{gs}	6.48 Ω
C_{gs_trench}	2.86e^{-15} F	C_{gd}	2.29e^{-14} F

R_{gd}	8.12 Ω	C_{gd_trench}	$7.31e^{-15}$ F
C_{ds}	$2.67e^{-14}$ F	g_{ds}	$1.01e^{-3}$ S
gm	$8.97e^{-3}$ S		

Table 5 The fitting error of the ps-model and the traditional model under (-1.6V, 10V) and (-3V, 15V)

error(ε)	(V_{gs}=-1.6V, V_{ds}=10V)		(V_{gs}=-3V, V_{ds}=15V)	
	The PS-model	The traditional model [2]	The PS-model	The traditional model [2]
ε(S_{11})	1.09 %	1.54 %	1.35 %	2.97 %
ε(S_{12})	2.29 %	2.99 %	2.24 %	2.68 %
ε(S_{21})	1.47 %	2.92 %	2.06 %	2.99 %
ε(S_{22})	1.02 %	1.37 %	1.45 %	1.99 %
ε(S)	1.47%	2.21%	1.78%	2.66%

In order to further verify the accuracy of the model, we extracted the model parameters of Fin-HEMT under 210 different bias points (V_{gs} is from -4 V to 0 V with the step of 0.2 V; V_{ds} is from 2 V to 20 V with the step of 2 V), and drew a three-dimensional diagram of the relationship between the model parameters and the change of V_{gs} and V_{ds}, where W_{Fin} is 300nm. In Figure 10(a), it is evident from the function C=Q/U that the C_{gs} are primarily influenced by the potential difference and charge between the gate and the source. As the V_{gs} rises, the device turns on and leads to an increase in charge under the gate, accompanied by a decrease in potential between the gate and the source. Therefore, C_{gs} increases with the increase of V_{gs}. The rise in V_{ds} contributes to an increase in source charge to a certain extent, leading to an upward trend in C_{gs}. However, it is noteworthy that the extent of this increase is confined within a limited range. In Figure 10(b), C_{gd} is affected by both the V_{gs} and the V_{ds}. The increase of the V_{gs} makes the device turn on to increase the amount of charge, and reduces the difference of potential between the gate and the drain, leading to an increasing C_{gd}. The increase in the V_{ds} will increase the potential difference between the drain and the gate, resulting in a decrease in C_{gd}. It can be seen from Figure 10(c) and (d) that the parasitic gm is smaller than the intrinsic gm due to the effect of the gate resistance. The variation of intrinsic gm with biases is the same as that of parasitic gm measured by DC, which exhibits excellent linearity at a high V_{ds}. The excellent linearity of Fin structure devices can be attributed to the increase of gate capacitance with V_{gs} [15].

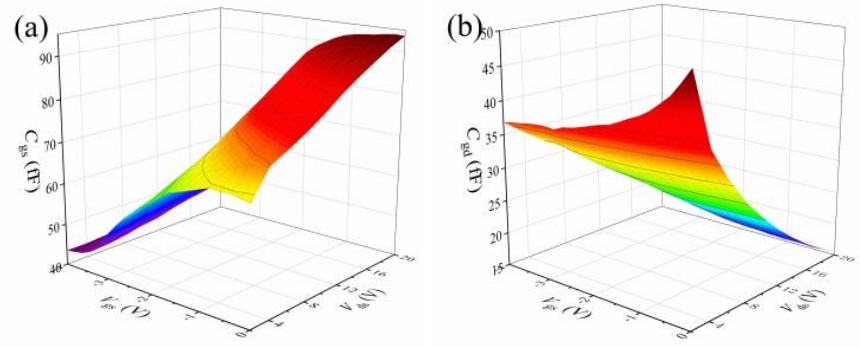

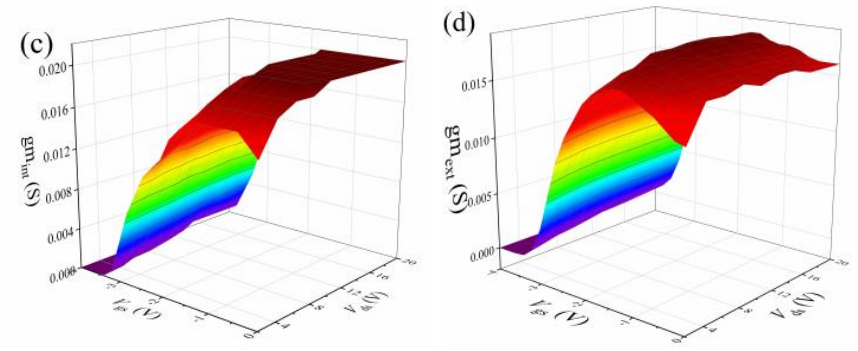

Figure 10 The 3-D graph for (a) The C_{gs} of the Fin-HEMT. (b) The C_{gd} of the Fin-HEMT. (c) The gm_{int} of the Fin-HEMT. (d) The gm_{ext} of the Fin-HEMT. The V_{gs} of the device is from -4 V to 0 V, and the V_{ds} is from 0 V to 20 V.

Next, C_{gs} and C_{gd} of devices with different Fin widths are analyzed in Figure 11. The C_{gs} and C_{gd} gradually increase with the increase of V_{gs}. As the decrease of Fin width, the overall trend of C_{gs} and C_{gd} is increasing. It has been proved that the gate capacitance increases with the decrease in W_{Fin} due to the improved side-wall gate control in narrower Fin structures [20]. This rule is consistent with the mechanism of the device and also proves the accuracy of the model.

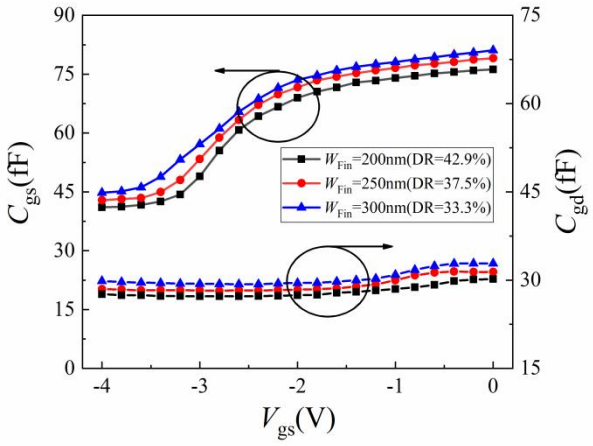

Figure 10 Comparison of the C_{gs} and C_{gd} among the Fin-HEMTs with 200 nm Fin Width, 250 nm Fin Width and 300 nm Fin Width.

5 Conclusion

In this work, a novel SSM (PS-model) for GaN Fin-HEMT is established. Based on the physical structure of the device, the PS-model introduces three new model parameters, C_g, C_{gs_trench}, and C_{gd_trench}, which are used to represent the capacitance generated between the Fin structure and 2DEG. Based on the actual process parameters of the device, the key parameters of the model are determined by Silvaco simulation. Because the new parameters have specific physical significance, parameter values can be calculated by the conformal transformation, which can quickly obtain parameter values and improve the efficiency and accuracy of model establishment. Finally, the PS-model can accurately fit the S-parameter of GaN-based Fin-HEMTs, and the fitting accuracy is better than 98%. At the same time, the change of key intrinsic parameters (C_{gs}, C_{gd}, and gm) with biases and the influence of different W_{Fin} on the model parameters were studied. Meanwhile, the trend and mechanism of parameter changes were explained, which further verified the

advancement and accuracy of the PS-model.

Acknowledgements This work was supported by the Fundamental Research Funds for the Central Universities under Grant XJSJ23053, Grant XJSJ23052, Grant ZYTS23026, and Grant XJS221113) and the National Natural Science Foundation of China under Grant 62234009 and Grant 62090014.

References

1 Shinohara et al. Scaling of GaN HEMTs and Schottky diodes for submillimeter-wave MMIC applications. IEEE Electron Device Lett., 2013, vol. 60, no. 10, pp. 2982–2996.
2 W. Shaobing, G. Jianfeng, W. Weibo, and Z. Junyun. W-band MMIC PA with ultrahigh power density in 100-nm AlGaN/GaN technology. IEEE Trans. Electron Devices., 2016, vol. 63, no. 10, pp. 3882–3886.
3 J. W. Chung, W. E. Hoke, E. M. Chumbes, and T. Palacios. AlGaN/GaN HEMT with 300-GHz fmax. IEEE Electron Device Lett., 2010, vol. 31, no. 3, pp. 195–197.
4 X. D. Liu et al. 1700 V High-Performance GaN HEMTs on 6-inch Sapphire With 1.5 μm Thin Buffer. IEEE Trans. Electron Devices., 2024, vol. 5, no. 1, pp. 84–87.
5 B. Romanczyk et al. W-Band Power Performance of SiN-Passivated N-Polar GaN Deep Recess HEMTs. IEEE Electron Device Lett., 2020, vol. 41, no. 3, pp. 349–352.
6 K. Ohi, J. T. Asubar, K. Nishiguchi, and T. Hashizume. Current stability in multi-mesa-channel AlGaN/GaN HEMTs. IEEE Trans. Electron Devices, 2013, vol. 60, no. 10, pp. 2997–3004.
7 K. Ohi and T. Hashizume, Drain current stability and controllability of threshold voltage and subthreshold current in a multi-mesa-channel AlGaN/GaN high electron mobility transistor, Jpn. J. Appl. Phys., 2009, vol. 48, no. 8R, p. 081002.
8 K. S. Im et al. High-performance GaN-based nanochannel Fin FETs with/without AlGaN/GaN heterostructure. IEEE Trans. Electron Devices, 2013, vol. 60, no. 10, pp. 3012–3018.
9 G. Crupi, D. Schreurs, B. Parvais, A. Caddemi, A. Mercha, and S. Decoutere. Scalable and multibias high frequency modeling of multi-Fin FETs. Solid State Electron., 2006, vol. 50, no. 11–12, pp. 1780–1786.
10 A. Majumder *et al.* Optimization of Small-Signal Model of GaN HEMT by Using Evolutionary Algorithms. IEEE MICROWAVE AND WIRELESS COMPONENTS LETTERS, 2017, vol. 27, no. 44, pp. 362–364.
11 F. Y. Huang *et al.* An Improved Small-Signal Equivalent Circuit for GaN High-Electron Mobility Transistors. IEEE Electron Device Lett., 2017, vol. 27, no. 4, pp. 362–364.
12 G. Crupi *et al*. High-Frequency Extraction of the Extrinsic Capacitances for GaN HEMT Technology. IEEE MICROWAVE AND WIRELESS COMPONENTS LETTERS, 2011, vol. 21, no. 8, pp. 445–447.
13 W. Y. Zhang *et al.* Novel Physics-Based Small-Signal Modeling and Characterization for Advanced RF Bulk FinFETs. IEEE Trans. Electron Devices, 2021, vol. 68, no. 5, pp. 2160–2166.
14 M. H. Mi *et al.* Millimeter-Wave Power AlGaN/GaN HEMT Using Surface Plasma Treatment of Access Region. IEEE Trans. Electron Devices, 2017, vol. 64, no. 12, pp. 4875–4881.
15 M. Zhang *et al.* Influence of Fin Configuration on the Characteristics of AlGaN/GaN Fin-HEMTs. IEEE Trans. Electron Devices, 2018, vol. 65, no. 5, pp. 1745–1752.
16 M. P. Sruthi *et al*. Analytical Model for Gate Capacitance and Threshold Voltage in Fin-Shaped GaN HEMTs. IEEE Trans. Electron Devices, 2021, vol. 68, no. 9, pp. 4793-4796.
17 M. P. Sruthi et al. Scalable Charge-Based Compact Model for Drain Current in Fin-Shaped GaN HEMTs. IEEE Trans. Electron Devices, 2023, vol. 70, no. 3, pp. 979- 985.
18 Y. Xiang. The electrostatic capacitance of an inclined plate capacitor. J. Electrostatics, 2006, vol. 64, no. 1, pp. 29–34.
19 Y. Xiang. Further study on electrostatic capacitance of an inclined plate capacitor. J. Electrostatics, 2008, vol. 66, nos. 7–8, pp. 366–368.
20 G. Dambrine *et al*. A new method for determining the FET small-signal equivalent circuit. IEEE Transactions on Microwave Theory and Techniques, 1988, vol. 36, no. 7, pp. 1151-1159.
21 A. Jarndal, and Kompa G. A new small-signal modeling approach applied to GaN devices. IEEE Transactions on Microwave Theory and Techniques, 2005, vol. 53, no. 11, pp. 3440-3448.
22 H. S. Zhang, *et al.* Influence of Different Fin Configurations on Small-Signal Performance and Linearity for AlGaN/GaN Fin-HEMTs. IEEE Transactions on Electron Devices, 2019, vol. 66, no. 8, pp. 3302-3309.
23 Y. He *et al*. Enhancement-mode AlGaN/GaN nanowire channel high electron mobility transistor with fluorine plasma treatment by ICP. IEEE Electron Devices Lett., 2017, vol. 38, no. 10, pp. 1421–1424
24 Z. Zhao et al. A fast small signal modeling method for GaN HEMTs. Solid-State Electron., 2020, vol. 175, Jan. 2021, Art. no. 107946.